A Building Block Assembly Dualband Dual-Polarized Antenna With Dual Wide Beamwidths for 5G Microcell Applications

BOTAO FENG[1], **(Senior Member, IEEE), JIEXIN LAI**[1],
AND CHOW-YEN-DESMOND SIM[2], **(Senior Member, IEEE)**
[1]College of Electronics and Information Engineering, Shenzhen University, Shenzhen 518060, China
[2]Department of Electrical Engineering, Feng Chia University, Taichung 40724, Taiwan

Corresponding author: Chow-Yen-Desmond Sim (cysim@fcu.edu.tw)

ABSTRACT A dualband dual-polarized antenna element with dual wide beamwidths for 5G microcell applications is initially proposed and investigated in this paper. To achieve very low manufacturing cost, an unprecedented method is applied to the antenna element, in which the antenna components are printed separately on F-4B substrates, follow by assembling them to form the antenna element (similar to building block assembly). To further achieve high gain, an 1×4 antenna array is also designed. Measured results show that the half power beamwidths (HPBWs) in H- and E-planes are $112\pm1°$ and $105\pm3°$ in the lower frequency band of 3.22-3.88 GHz, respectively, and $99\pm3°$ and $106\pm4°$ in the upper frequency band of 4.52-5.02 GHz, respectively. In addition, high front-to-back ratio (FBR) of approximately 19 dB and high isolation of 33.6 dB can also be achieved.

INDEX TERMS Building block assembly, dualband, dual-polarized, dual wide beamwidths, 5G microcell applications.

I. INTRODUCTION

Since 2019, the fifth generation mobile communication (5G) has entered the stage of rapid development as commercial licences are formally issued to the telecommunication operators in many countries [1]. Amid the key components of 5G system, the antenna has played an increasingly important role in system performance. For example, to satisfy the stringent requirements including high-speed transmission and high capacity in wide coverage area, strong anti-interference capability, limited storage space, etc. for 5G communication, the antennas involved should own the corresponding high-performance characteristics such as high gain and wide beamwidth, high isolation at low cost, small size, etc. [2]–[4]. In addition, because the communication wavelength of 5G deployment below 6-GHz (also known sub-6 GHz band) are shorter than that of previous mobile communication systems, the demand for microcell antenna that can be used for medium and short distances communication

The associate editor coordinating the review of this manuscript and approving it for publication was Yasar Amin.

has surged across emerging markets. Recently, several antennas for microcell application with good performances have been proposed [5], [6], however, the above-mentioned multiple high-performance characteristics have not been properly taken into account.

For practical application, a microstrip antenna can be completely printed on a common substrate and assembled within a short time period. Because of its advantages such as low fabrication cost, high production efficiency and high manufacturing accuracy etc., since its invention, the microstrip antenna (printed on substrate) is widely used today. However, most of the microstrip antennas are planar structure and cannot be applied in three-dimensional (3D) construction [7]. In reality, base-station and microcell antennas are mostly fabricated with 3D construction because it can yield both wide bandwidth and high gain easily [8]–[11]. Recently, several microstrip antennas with 3D construction have been proposed for base-station and microcell applications [12], [13]. In [12], the 3D antenna units and its corresponding feeding network are printed on substrates and arranged in a loop array, resulting with a high gain of 10.3 ± 0.9 dBi and

a low gain variation within 1.25 dB in the horizontal plane. In [13], a vertical parasitic superstrate is employed in the dual-polarized linear array to compensate the impedance variation in beam scanning cases. As a result, the weight of the array can be effectively reduced while wide scanning angle of approximately 120° can be achieved. Though excellent performances have been realized, their frequency bandwidths are not suitable for 5G communications.

As is well known, antennas with wide beamwidth can help to cover much wider area with fewer antenna numbers and they are also beneficial to the efficient use of resources. By properly adjusting the antenna radiation pattern of microcell, the mobile users can receive vast amount of information from the microcell in a very short time. To achieve this goal, many works with various methods have been reported [6], [14], [15]. In [14], by folding the planar ground into a trapezoid-shaped one, the electric dipole of a single polarized ME-dipole antenna inclines toward the ground and its beamwidth in H-plane reaches to 120° with approximately 6.3 dBi. In [15], by folding the electric dipole of a single polarized ME-dipole antenna toward the ground and arranging six metal cylinders around it, HPBWs of 215° and 186° in the E- and H-planes, respectively, can be obtained for 5.5 GHz at the same time. Furthermore, by integrating a modified tetrahedral ground together with dual-layer three-element dipoles that are arranged as a triangle array, dual wide HPBWs of 163° and 133° in H-plane can be achieved in dual-polarized directions [6]. Nevertheless, up to now, few works in the open literatures have simultaneously realized wide E- and H-planes in each polarization for dual-polarized antennas due to the challenging technical difficulty. In fact, dual-polarized antennas are most widely used in microcell communication as it can double the system capacity without increasing the size and combat multipath interferences significantly [16]. Therefore, dual-polarized antennas with dual wide beamwidths are in urgent need for 5G communication scenarios.

On the other hand, high isolation in a compact size is always a challenging research topic for dual-polarized antennas. So far, many studies with great efforts have been made in this aspect [17], [18]. In [17], by placing four V-shaped patches around the radiating patches and introducing orthogonal feeding scheme, high isolation of better than 25 dB with a compact size of $40 \times 40 \times 1.524$ mm^3 can be achieved in the bandwidth of 3.0-4.1 GHz. Furthermore, in [18], by using a differential feeding network to excite dual-polarized magnetic dipole antenna, high isolation of larger than 45 dB with wide beamwidth of 133° can be realized in the bandwidth of 5.1-5.8 GHz. However, its profile is slightly high ($0.32\lambda_0$). In addition to that, low fabrication cost is also a very important consideration. Hence, differential feeding network that may increase the fabrication cost is not the best option for practical application.

As stated above, even though there is a trade off among the high gain and wide beamwidth, isolation and compact size, high fabrication precision and low cost, other vital requirements for 5G communications are also needed to be satisfied besides the above mentioned multiple high-performances. To address these requirements, we roughly presented a simulated wideband dual-polarized antenna element with wide beamwidths in [19]. However, it still suffers from low gain, unstable beamwidth in both radiation planes and slightly larger size due to the design flaw of the fence. In this paper, a dualband dual-polarized antenna element with dual wide beamwidths for 5G microcell applications is initially studied. To achieve low cost and ease in manufacturing with high precision, all the antenna components (the radiating patch, two shorted walls, ground plane, four fences, and four feeding lines that form the ME dipole) are separately printed on low cost F-4B substrates and the antenna element can be easily assembled like building blocks. The final assembled antenna element is a dual-feed type (with high isolation of 33.6 dB) that has a small size of $0.4 \times 0.4 \times 0.134$ λ_0^3. Besides exhibiting dual wide bandwidths of 18.6% (3.22-3.88 GHz) and 11.1% (4.52-5.02 GHz), dual wide half-power beamwidths (HPBWs) of approximately 100° are also yielded. To further achieve high gain, an 1×4 antenna array is designed, whose gain of larger than 10.3 dBi can be simultaneously achieved for both ports. With these steps, the proposed antenna element is suitable for the practical 5G microcell communications.

II. ANTENNA ELEMENT
A. ANTENNA ELEMENT CONFIGURATION AND WORKING PRINCIPLE

Fig. 1 and Table 1 show the detailed configuration and dimensions of proposed dual-polarized antenna element, respectively. For validation purposes, the corresponding antenna prototype is fabricated as shown in Fig. 2.

As shown in Fig. 1(a), all the components of the antenna element are printed on F-4B substrate with a thickness of 1 mm ($\varepsilon_r = 3.5$ and $\tan\delta = 0.007$), and the bonding between two related components are via their corresponding protruded joint section and narrow slot. By doing so, the antenna element can be quickly assembled like building blocks. In other words, both high efficiency and high precision can be simultaneously achieved at low cost. As is well known, a typical dual-polarized ME-dipole antenna consists of two pairs of horizontally arranged electric dipoles, two pairs of corresponding vertically placed magnetic dipoles, a pair of orthogonal η-shaped feedlines and a square ground. Among them, the magnetic dipoles are comprising of four vertical shorted patches (namely shorted wall) and the ground between them. To achieve our design goals, there are several modifications as follows:

(1) As shown in Figs. 1(a) and 1(b), by cutting off the patch corners (of size $W_2 \times W_3$) of the adjacent electric dipoles, better impedance matching with wide bandwidth can be easily achieved.

(2) The construction of the two feeding lines are as shown in Figs. 1(b) and 1(e). The sections related to Port 1 and
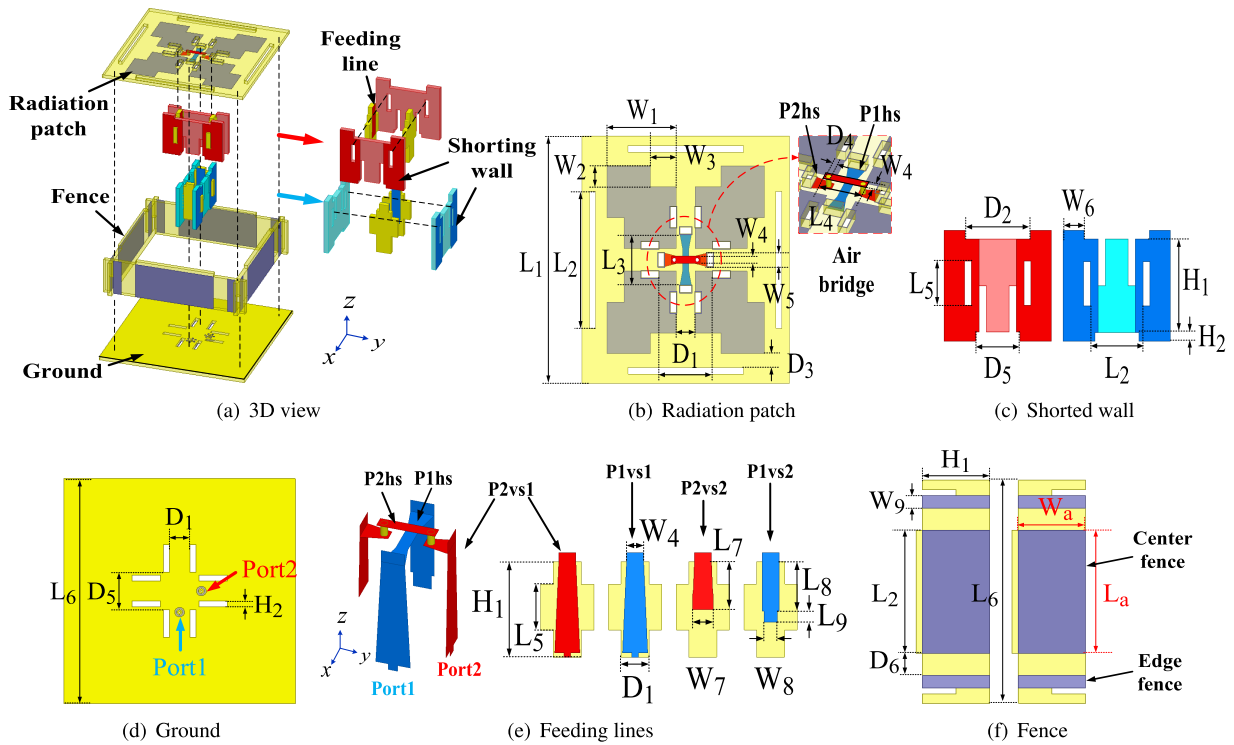
FIGURE 1. Geometry of the proposed antenna.

TABLE 1. Geometrical parameters of the antenna element (Unit: mm).

Parameter	L_1	L_2	L_3	L_4	L_5	L_6	L_7	L_8
Value	36	20	7.5	5	5	37.3	5.2	5.4
Parameter	L_9	L_a	W_1	W_2	W_3	W_4	W_5	W_6
Value	1.2	20	12	3	4.5	1	2	3
Parameter	W_7	W_8	W_9	W_a	D_1	D_2	D_3	D_4
Value	2.4	1.56	2	10.5	3.3	9.4	2	0.6
Parameter	D_5	D_6	H_1	H_2				
Value	6.3	3.65	10.5	1				

FIGURE 2. Photographs of the antenna element.

Port 2 are indicated in blue color and red color, respectively. Here, the vertical section 1 of Port 1 (P1vs1) is linked to the vertical section 2 of Port 1 (P1vs2) via the horizontal section of Port 1 (P1hs) that is printed on the same surface as the radiating patch. As for the vertical section 1 of Port 2 (P2vs1), it is linked to the vertical section 2 of Port 2 (P2vs2) via an air bridge (P2hs). Notably, this air bridge is built by a printed rectangular strip P2hs ($L_4 \times W_4$) with its two open-ends each shorted to a small isosceles trapezoid patch through a small cylindrical via of diameter 0.6 mm (D_4). The two small trapezoid patches are printed alongside (same surface) with the radiating patch and P1hs, whereas the rectangular strip is printed on the other surface of the substrate. Thus, the gap of the air bridge is the same as the substrate thickness of 1 mm. Consequently, the isolation between the two input ports can be significantly improved.

(3) As shown in Figs. 1(a) and 1(f), four fences are vertically arranged to surround the modified dual-polarized ME dipole antenna. The planar size of each fence is
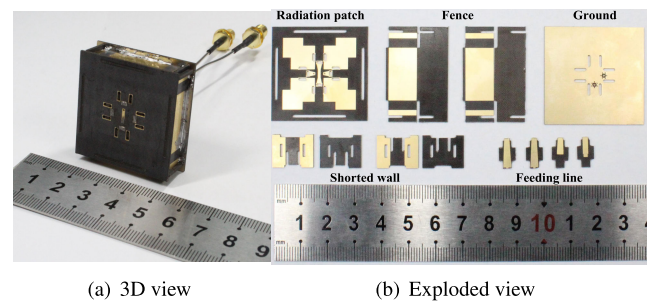
37.3×10.5 mm^2 ($L_6 \times H_1$), disregarding the two extended sides that are used to hold/bond the four fences vertically and firmly together. Here, each fence is composed of a large center rectangular patch ($L_a \times W_a$, also known as center fence) with two narrow rectangular strips ($W_8 \times W_a$, also known as edge fence) printed on its two sides with a gap distance of 3.65 mm (D_6). The main reason for having these four fences are because of their existence together with the above modified electric dipoles of ME-dipole antenna can yield dual wide HPBWs of approximately 100° as well as small size of $0.4 \times 0.4 \times 0.134 \lambda_0^3$. Owing to the employment of the fences, the backward electromagnetic radiation can be also suppressed. As a result, high FBR and gain enhancement are correspondingly obtained.

To depict the working principle of the dual wide beamwidths, Fig. 3 exhibits the ideal concept graphs between the current distribution and the radiation pattern. As observed in XOZ-plane (side view), a broadside radiation with wide
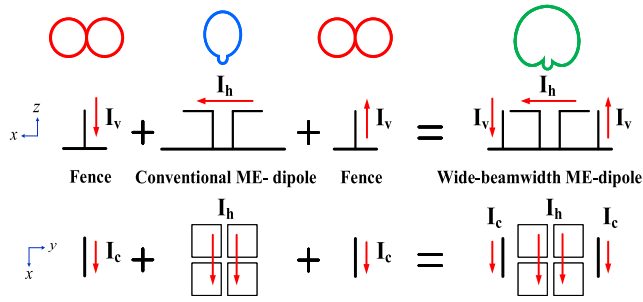
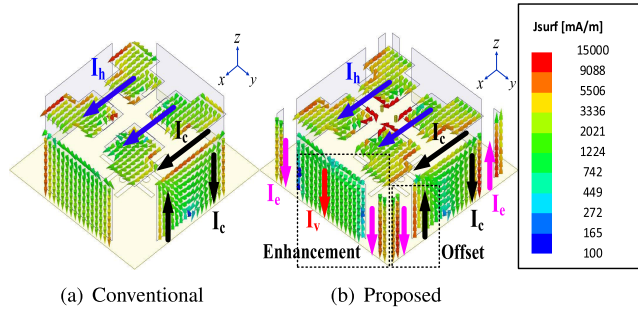**FIGURE 3.** Working principle of the dual wide beamwidths.

(a) Conventional   (b) Proposed

FIGURE 4. Comparison of current distributions on different antennas for port 1 at 4.9 GHz.

FIGURE 5. The effect of the fence height W_a at 4.9 GHz.

3-dB beamwidth is yielded because of the incorporation between the directional radiation pattern (excited by the horizontal current I_h flowing on the patch surfaces of electric dipole) and the 8-shaped radiation pattern (generated by the upward currents I_v flowing on the center fence). Likewise, horizontal currents I_h flowing on the patch surfaces of the electric dipoles incorporated with the currents I_c flowing on center fence will constitute another wide 3-dB beamwidth radiation in the XOY-plane (top view). Therefore, dual wide beamwidths can be simultaneously achieved by the proposed modified ME-dipole element. According to [15], the normalized radiation patterns of the proposed antenna element in E-plane and H-plane ($F_E(\theta)$, $F_H(\theta)$) can be described as follows:

$$F_E(\theta) = F_H(\theta)$$
$$= 1 + Bsin\theta \qquad (1)$$

where B is the complex coefficient that is decided by the parameters of the vertical center and edge fences. Here, as both B and $sin\theta$ are positive real number, $F_E(\theta)$ is larger than 1.

Fig. 4 further shows simulated current distributions on the proposed electric dipoles and fences for port 1 at 4.9 GHz. As can be seen from Fig. 4(a), with the conventional fence that consists of single center fence only, the beamwidth in YOZ-plane is much wider than the one in XOZ-plane. By using the proposed fences, wide beamwidth in the YOZ-plane can also be achieved by incorporating the radiations excited by I_h and I_c. Notably, the directions of the currents on the edge fences (I_e, in purple) along the XOZ-plane are opposite to that of vertical portion of I_c, whereas the directions of I_e along the YOZ-plane are the same as the
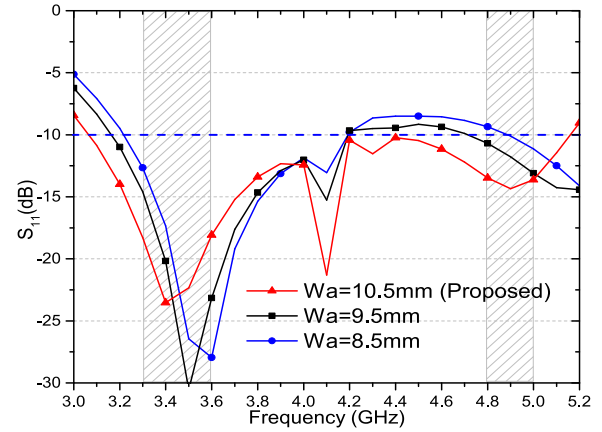
directions of I_v flowing on the center fence. That is to say, the current intensity in the XOZ-plane is slightly reduced whereas the one in the YOZ-plane is increased. As a result, the 3-dB beamwidths in the XOZ-plane and YOZ-plane can be broadened at the same time when port 1 is excited. Owing to symmetrical structure, the situation of port 2 is similar to that of port 1. For brevity, it is not given here.

B. SIMULATED AND MEASURED RESULTS

In order to achieve optimal antenna performance, some key parameters and different structures are compared using the electromagnetic simulation software *ANSYS HFSS* [20]. In addition, measured results of the antenna prototype are also used to verify the correctness of simulation results.

Fig. 5 shows the effect of the fence height W_a at 4.9 GHz for port 1. As displayed, the resonant points at both the lower and upper desired frequencies move toward the lower spectrum when increasing W_a, which indicates that the fence is also partial of the radiator besides the ME-dipole. After optimization, W_a is selected as 10.5 mm to cover the desired dual bandwidths for 5G sub-6 GHz. Similarly, Fig. 6 shows the effect of tuning the fence length W_a on beamwidths at 4.9 GHz for port 1. When L_a increases from 16 mm to 24 mm with an interval of 4 mm, as shown in Fig. 6(a), the beamwidth in the E-plane becomes narrow. In contrast, as depicted in Fig. 6(b), the beamwidth in the H-plane becomes much wider with increasing L_a. To guarantee wide beamwidths in both planes, $L_a = 20$ mm is chosen as the optimum value.

Fig. 7 shows the effect of applying different fences on both radiation planes at 4.9 GHz for port 1. Without the fence, the HPBWs in both E- and H-plane are 66.4° and 78.2°, respectively, and they are the narrowest. With only two pieces of center fences, the HPBWs in both E- and H-planes become wider at 163.3° and 120.1°, respectively. As they are not close to each other, the FBR in both planes becomes deteriorated and reduces to approximately 6.43 dB. In contrast, with four pieces of center fences, the HPBW in E-plane is 109.2° and becomes slightly narrow, whereas the HPBW in H-plane is significantly wider at 234.2°,
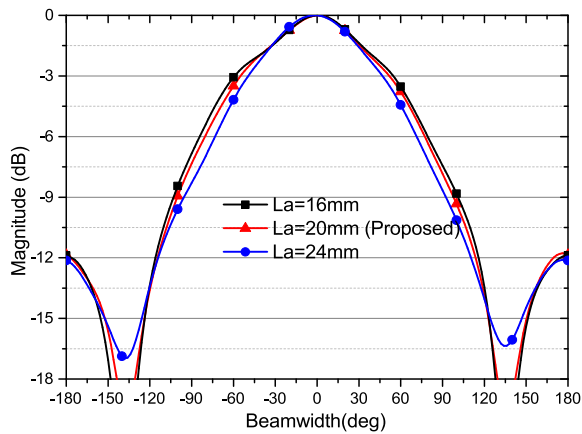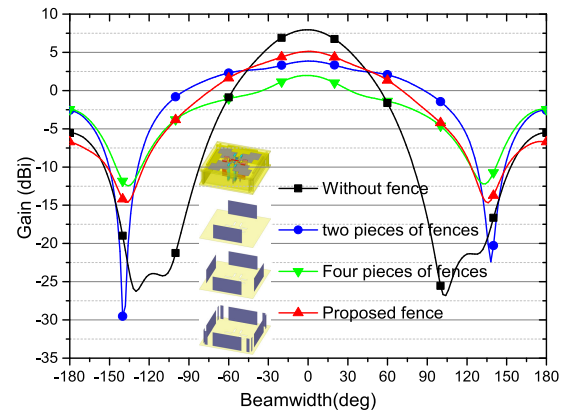
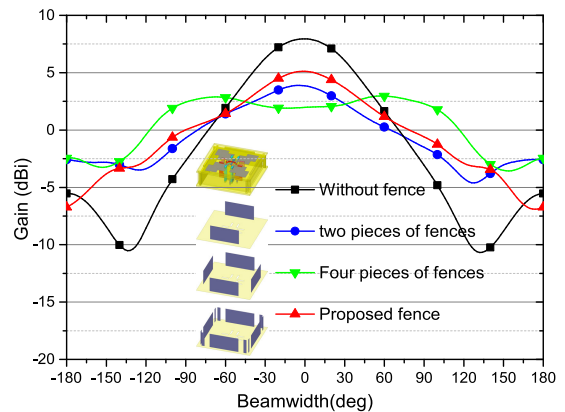(a) E-plane radiation pattern
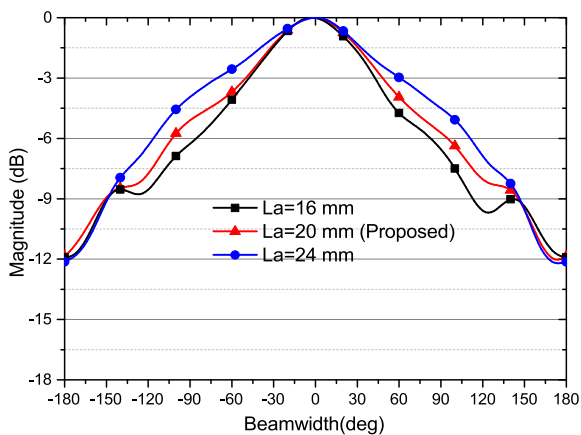
(b) H-plane radiation pattern

FIGURE 6. The effect of the fence width L_a at 4.9 GHz.

(a) E-plane radiation pattern

(b) H-plane radiation pattern

FIGURE 7. The effect of different fences on both radiation planes at 4.9 GHz for port 1.

likewise, the HPBWs in both radiation planes are not close to each other and the FBR further falls to approximately 4.42 dB. Consequently, the peak gains in E- and H-planes have reduced to 1.98 dBi and 2.88 dBi, respectively. With the proposed fence, the HPBWs in E- and H- planes are 106.7° and 98.2°, respectively. In addition, the corresponding FBRs in both radiation planes are approximately 11.8 dB, and their peak gain reach to 5.12 dBi. In comparison, stable wide HPBWs, high gain as well as high FBR can be simultaneously achieved in both radiation planes with the proposed fence.

Fig. 8 shows the simulated and measured S-parameters and gains for both ports. As exhibited, the simulated S_{11} is ranging from 3.05 GHz to 5.15 GHz, while the measured S_{11} varies from 3.22 GHz to 3.88 GHz, and from 4.16 GHz to 5.05 GHz for port 1, respectively. Correspondingly, the simulated and measured gains are 5.33±0.05 dBi and 5.16±0.05 dBi, respectively. Likewise, the simulated S_{22} is ranging from 3.03 GHz to 5.15 GHz, while the measured S_{22} varies from 3.25 GHz to 3.93 GHz, and from 4.52 GHz to 5.15 GHz, respectively. Their corresponding gains are 5.09±0.01 dBi and 4.95±0.04 dBi. In other words, the overlapped simulated bandwidth is 3.05-5.15 GHz with gain of 5.2±0.2 dBi, while the overlapped measured ones are

3.25-3.88 GHz and 4.52-5.05GHz with gain of 5.25±0.2 dBi, respectively. The measured results are slightly inferior than the simulated ones due to the measured errors caused by transmission cables and connectors. As shown in Fig. 9, owing to the air bridge design, the simulated and measured S_{21} for both ports are less than −34.9 dB and −31.8 dB within the desired frequency bands, indicating excellent isolation between both polarization. For a conventional dual-polarized microcell antenna, isolation larger than 25 dB meets the anti-interference requirement. Though there are some measured errors between the curves, their curvilinear trends are basically the same.

Fig. 10 and Table 2 exhibit the corresponding radiation patterns and characteristics at 3.5 GHz and 4.9 GHz for both ports. Here, for port 1, its E-plane and H-plane correspond to XOZ-plane and YOZ-plane, respectively. It is the opposite for port 2. For port 1 at 3.5 GHz, the simulated HPBW, cross polarization (X-pol) level and FBR in the XOZ plane are 105.9°, −28.5 dB and 13.5 dB respectively. As for those in the YOZ-plane, they are 112.8°, −34.4 dB and 13.5 dB, respectively. In comparison, the measured ones are 108°, −21.9 dB and 25.5 dB, respectively, in the XOZ plane, and 110°, −21.3 dB and 25.3 dB, respectively, in YOZ-plane. Similarly, at 4.9 GHz, the simulated HPBW, X-pol
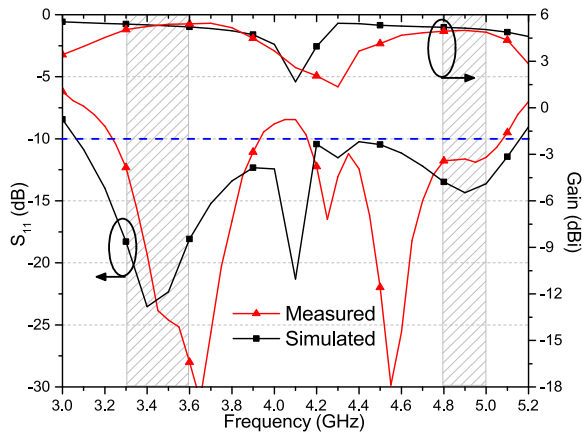
(a) S_{11} and gains for port 1
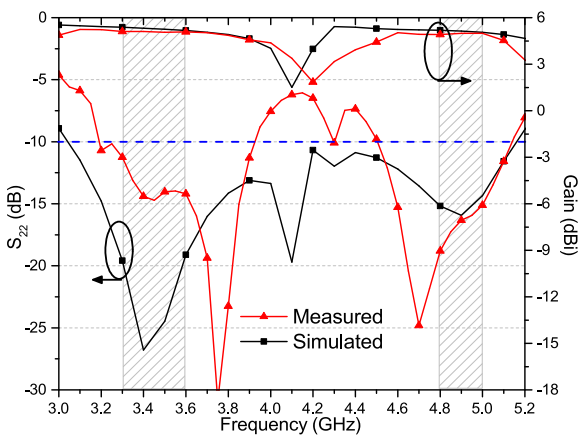
(b) S_{22} and gains for port 2

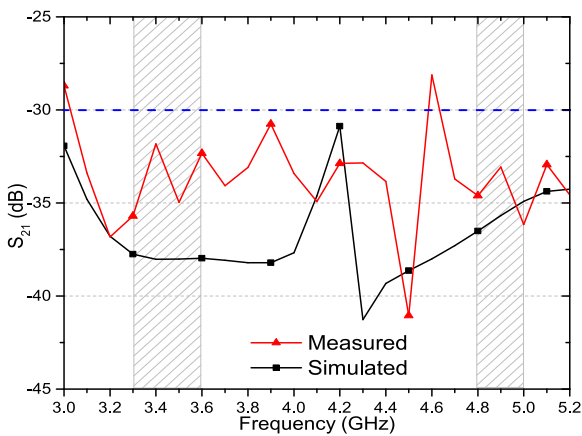**FIGURE 8.** Simulated and measured S-parameters and gains for both ports.

FIGURE 9. S_{21}.

(a) 3.5 GHz for port 1   (b) 4.9 GHz for port 1

(c) 3.5 GHz for port 2   (d) 4.9 GHz for port 2

— E-plane-Sim Co-pol ; – ✕ · E-plane-Mea Co-pol
— H-plane-Sim Co-pol ; – – – H-plane-Mea Co-pol
— E-plane-Sim X -pol ; – • – E-plane-Mea X -pol
— H-plane-Sim X- pol ; – ▽ – H-plane-Mea X -pol

FIGURE 10. Simulated radiation patterns of the antenna element at 3.5 and 4.9 GHz for both ports.

TABLE 2. Radiation performances of the antenna element at different frequencies.

Parameter	Port 1					
	XOZ-plane			YOZ-plane		
Frequency (GHz)	HPBW (deg)	X-pol (dB)	FBR (dB)	HPBW (deg)	X-pol (dB)	FBR (dB)
3.5 (Simulated)	105.9	-28.5	13.5	112.8	-34.4	13.5
3.5 (Measured)	108	-21.9	25.5	110	-21.3	25.3
4.9 (Simulated)	106.7	-33.7	11.8	98.2	-20.5	20.6
4.9 (Measured)	98	-20.5	20.6	101	-20.2	19.9
	Port 2					
3.5 (Simulated)	112.3	-30.1	13.4	105.3	-35.7	13.4
3.5 (Measured)	109	-22.5	20.1	106	-21.7	19.8
4.9 (Simulated)	98.3	-20.3	12.1	106.5	-30.1	12.1
4.9 (Measured)	97	-36.1	19.2	108	-20.5	18.9

In general, the measured results are analogous to the simulated ones, and they show dual wide beamwidths in E- and H-planes, low cross polarization and acceptable FBR.

III. DUAL LINEARLY POLARIZED ANTENNA ARRAY

In order to obtain high gain for long distance transmission, an 1×4 dual linearly polarized antenna array is proposed and fabricated, as shown in Figs. 11 and 12.

The proposed antenna array is realized by assembly four antenna elements to a meticulously designed dual-polarized feeding network, as shown in Figs. 11(a) and 11(b), respectively. The four antenna elements are arranged in parallel and the center distance between the adjacent elements is 0.5 λ_0 (47.3 mm, λ_0 is the free-space wavelength at the starting frequency). The feeding network is composed of two

level and FBR in the XOZ plane are 106.7°, −33.7 dB and 11.8 dB, respectively. As for those in the YOZ-plane, they are 98.2°, −36.2 dB and 11.8 dB, respectively. Correspondingly, the measured ones are 98°, −20.5 dB and 20.6 dB, respectively, in XOZ-plane, and 101°, −20.2 dB and 19.9 dB, respectively, in YOZ-plane. The conditions of port 2 are similar to port 1 due to the nearly symmetrical structure.
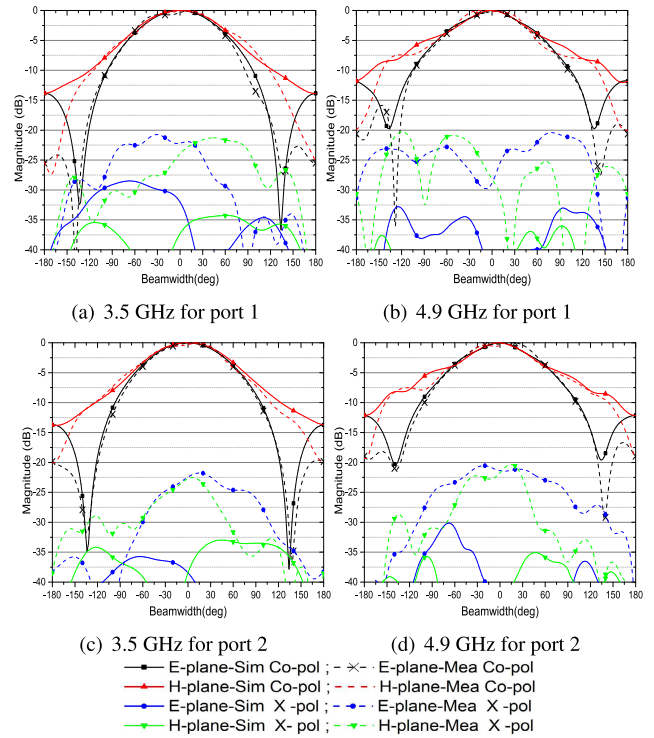
TABLE 3. Radiation performances of the antenna array at different frequencies.

Parameter	Port 1						Port 2					
	XOZ-plane			YOZ-plane			XOZ-plane			YOZ-plane		
Frequency (GHz)	HPBW (deg)	X-pol (dB)	FBR (dB)	HPBW (deg)	X-pol (dB)	FBR (dB)	HPBW (deg)	X-pol (dB)	FBR (dB)	HPBW (deg)	X-pol (dB)	FBR (dB)
3.5 (Simulated)	108.9	-34.6	14.5	23.2	-25.7	14.5	93.8	-24.5	24.1	20.9	-28.6	24.1
3.5 (Measured)	113	-21.7	20.4	24	-22.4	22.1	104	-23.7	27.4	25	-21.8	26.9
4.9 (Simulated)	100.5	-36.1	14.7	17.7	-20.8	14.7	102.2	-21.7	20.7	17.2	-20.5	20.7
4.9 (Measured)	102	-21.4	19.2	17	-20.7	20.1	103	-20.2	24.1	18	-21.1	21.6

TABLE 4. Characteristics and performances comparison of proposed antenna with Other referenced wide-beamwidth antenna elements.

Refs.	Polarization	Bandwidth (Relative BW/GHz)	Size (λ_0^3 / mm^3)	HPBW H-plane (deg)	HPBW E-plane (deg)	FBR (dB)	Isolation (dB)	Remarks
[14]	Single LP	45.4% (2.37-3.76)	0.79×0.78×0.33 / 100×98.8×41.9	118±5	73±5	15	N.A.	Wide bandwidth; Stable wide H-plane; High FBR; Large size; Single LP.
[15]	Single LP	81.1% (3.3-7.8)	0.44×0.44×0.176 / 40×40×16	83-186	106-217	8.5	N.A.	Wide bandwidth; Unstable wide E/H-plane; Small size; Low FBR; Single LP.
[22]	Single LP	62.6% (2.16-4.13)	0.83×0.83×0.216 / 115×115×30	40-107	35-191	8	N.A.	Wide bandwidth; Unstable wide E/H-plane; Low FBR; Large size; Single LP.
[18]	Dual LP	4.5% (5.02-5.23)	1.33×1.33×0.03 / 80×80×2	125	110	N.A.	22	Narrow bandwidth; Stable wide E/H-plane; High FBR; Small size; Dual LP.
[6]	Dual LP	22.6% (3.25-4.08) & 19.6% (4.29-5.22)	0.7×0.7×0.37 / 63.3×63.3×33.4	83-162	91-168	24 13	31	Dual bandwidth; Unstable wide E/H-plane; High FBR; High isolation; Large size; Dual LP.
Proposed element	Dual LP	18.6% (3.22-3.88) & 11.1% (4.52-5.02)	0.4×0.4×0.134 / 37.3×37.3×12.5	112±1; 99±3	105±3 106±4	19.8 18.9	33.6	Dual bandwidth; Stable wide E/H-plane; High FBR; High isolation; Small size; Dual LP.

where λ_0, LP, N.A. denote the free-space wavelength at the starting frequency, linear polarization, not available, respectively.

(a) 3D view

(b) Feeding network

FIGURE 11. Geometry of the dual linearly polarized antenna array.
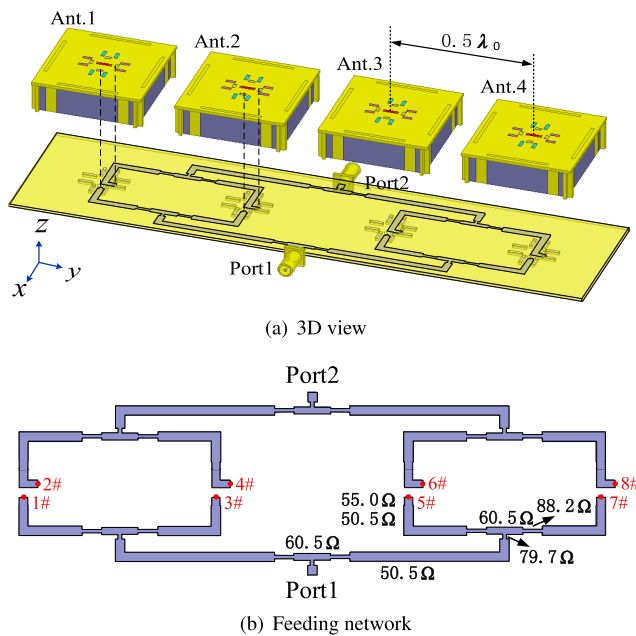

FIGURE 12. Photograph of the dual linearly polarized antenna array.

dual-layer 1-to-2 power divider networks. The detailed impedance matchings are marked in Fig. 11(b). Each pair of output ports of the feeding network in the same column (i.e. 1# and 2#) connect to the two input ports of each corresponding antenna element. According to [21], the normalized
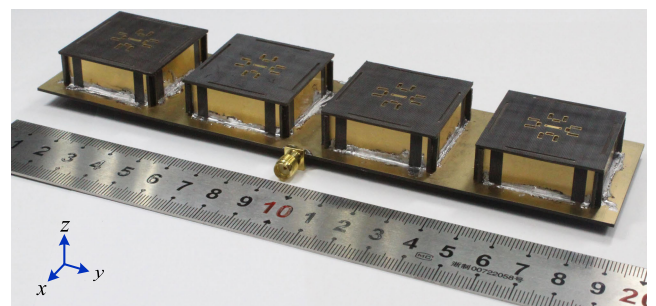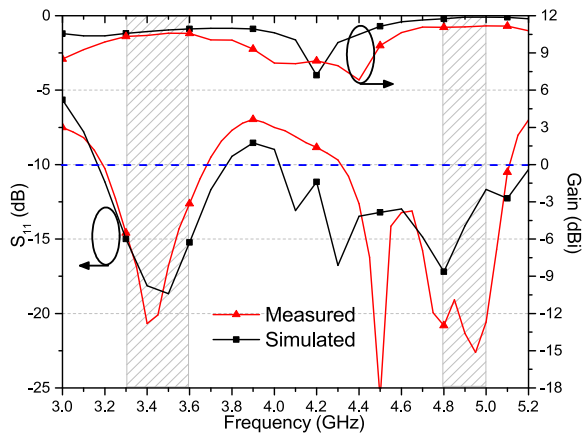
radiation patterns of the proposed antenna array in YOZ-plane ($F_{YOZ}(\theta)$) for port 1 can be described as follows:

$$AF = \sum_{n=1}^{N} e^{j(n-1)(kd\cos\theta + \beta)}$$

$$= \sum_{n=1}^{N} e^{j(n-1)(kd\cos\theta)} \qquad (2)$$

$$F_{YOZ}(\theta) = F_E(\theta) \cdot AF$$

$$= (1 + B\sin\theta) \cdot \sum_{n=1}^{4} e^{j(n-1)(kd\cos\theta)} \qquad (3)$$

where AF is the array factor, $F_E(\theta)$ represents the E-plane radiation pattern of each antenna element, k denotes the

(a) S_{11} and gains for port 1
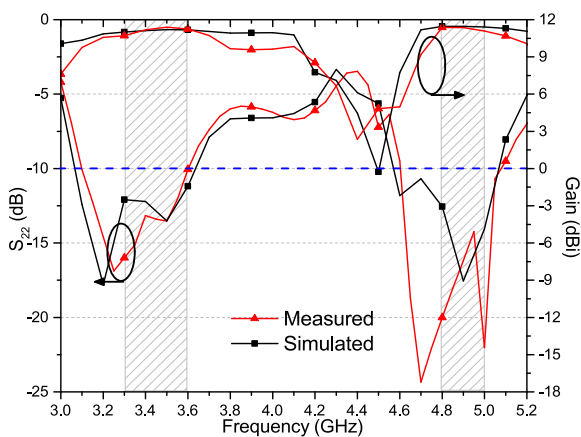
(b) S_{22} and gains for port 2

FIGURE 13. Simulated and measured S-parameters and gains for both ports.

FIGURE 14. S_{21}.

(a) 3.5 GHz for port 1   (b) 4.9 GHz for port 1

(c) 3.5 GHz for port 2   (d) 4.9 GHz for port 2

E-plane-Sim Co-pol ; – ✕ – E-plane-Mea Co-pol
H-plane-Sim Co-pol ; – – H-plane-Mea Co-pol
E-plane-Sim X -pol ; – • – E-plane-Mea X -pol
H-plane-Sim X- pol ; – ▼ – H-plane-Mea X -pol

FIGURE 15. Simulated radiation patterns of the antenna array at 3.5 and 4.9 GHz for both ports.

wave numbers, d and β are the separation and the phase difference between adjacent antenna elements, respectively. Here, each antenna element is fed in phase and hence $\beta = 0°$. Therefore, compared with the radiation pattern of a single antenna element, there are obvious changes in the YOZ-plane radiation pattern of the antenna array. To verify our design, both simulation and measurement are also carried out.

As shown in Fig. 13, the simulated dual bandwidths ($S_{11} \leqslant -10$ dB) for port 1 are ranging from 3.17 GHz to 3.73 GHz, and from 4.00 GHz to 5.23 GHz, respectively, with gain of 11.22±0.66 dBi. Correspondingly, the measured ones are varying from 3.15 GHz to 3.67 GHz, and from 4.35 GHz to 5.12 GHz, respectively, with gain of 10.76±0.43 dBi. Similarly, for port 2, they are varying from 3.05 GHz to 3.62 GHz, and from 4.57 GHz to 5.06 GHz ($S_{22} \leqslant -10$ dB), with gain of 11.27±0.28 dBi for simulated results, respectively. The corresponding measured ones are from 3.11 GHz to 3.62 GHz, and from 4.62 GHz to 5.05 GHz, respectively, with gain of 11.04±0.33 dBi. That is to say, the simulated overlapped impedance bandwidths for the two input ports of the dual LP antenna array are 13.3% (3.17-3.62 GHz)
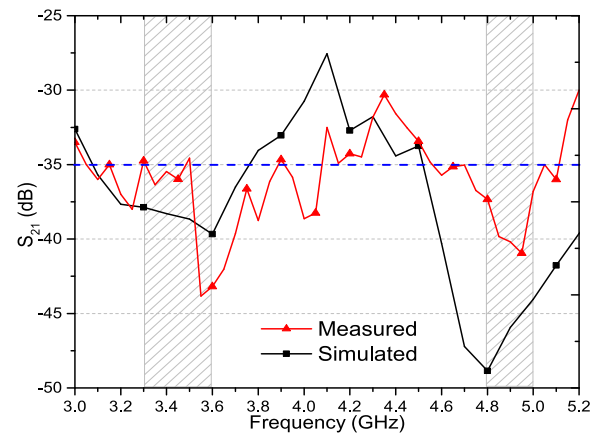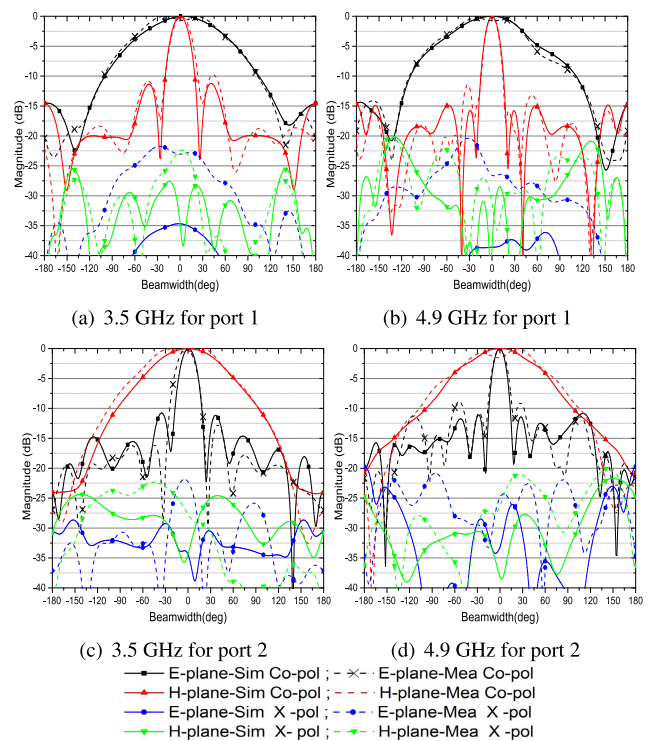
and 10.2% (4.57-5.06 GHz), and the measured overlapped ones are 13.9% (3.15-3.62 GHz) and 8.9% (4.62-5.05 GHz) ($S_{11} \leqslant -10$ dB, $S_{22} \leqslant -10$ dB), with gain of 11.22±0.66 dBi. As shown in Fig. 14, the simulated and measured S_{21} for both ports are below -34.7 dB and -36.8 dB within the desired frequency bands, which also shows excellent isolation between two input ports. In addition, their curvilinear trends are well consistent with each other.

Fig. 15 and Table 3 display the antenna array radiation patterns and characteristics at 3.5 GHz and 4.9 GHz for both ports. Likewise, the E- and H-planes for port 1 correspond to XOZ- and YOZ-planes, respectively. It is also the opposite

to port 2. For port 1 at 3.5 GHz, the simulated HPBW, X-pol level and FBR in the XOZ-plane are 108.9°, −34.6 dB and 14.5 dB, respectively. As for the ones in the YOZ-plane, they are 23.2°, −25.7 dB and 14.5 dB, respectively. In comparison, the measured ones in the XOZ-plane are 113°, −21.7 dB and 20.4 dB, respectively, and in the YOZ-plane are 24°, −22.4 dB and 22.1 dB, respectively. Similarly, at 4.9 GHz, the simulated HPBW, X-pol level and FBR are 100.5°, −36.1 dB and 14.7 dB in the XOZ-plane, respectively, and 17.7°, −20.8 dB and 14.7 dB in the YOZ-plane, respectively. Correspondingly, the measured ones are (102°, −21.4 dB and 19.2 dB) and (17°, −20.7 dB and 20.1 dB) in the XOZ- and YOZ-planes, respectively. The conditions of port 2 are also similar to port 1 due to the symmetrical structure. Compared with the antenna element, the results confirm that significant changes in the beamwidth have yielded. On the whole, the measured results agree well with the simulated ones, and they show wide beamwidth along y-axis, low cross polarization and acceptable FBR.

IV. COMPARISON AND DISCUSSIONS

Table 4 displays the main characteristics and performances of the proposed antenna element, and they are compared with other referenced wide beamwidth antenna elements. In comparison, the proposed antenna element has exhibited dual stable wide beamwidths, smaller planar size, higher isolation, and higher FBR. Though the bandwidth is not superior to others, it can still cover the desired 5G sub-6 GHz frequencies. As discussed above, the proposed antenna element with these characteristics may meet the stringent demands including wide coverage area, good anti-interference ability and compact size, etc. for 5G sub-6 GHz communication scenarios. In addition, though only a wide beamwidth can be realized for each polarization for 1 × 4 antenna array at a time, high gain of 11.22±0.66 dBi can be achieved which guarantees long distance transmission.

V. CONCLUSION

A dualband dual-polarized antenna element with dual wide beamwidths has been successfully studied in this paper. Here, an unprecedented method to build the antenna element is also introduced, in which all antenna components are printed on low cost F-4B substrate and can be easily assembled (analogous to building block assembly) with high precision. By arranging four meticulously designed fences surrounding the modified dual-polarized ME-dipole antenna, dual wide HPBWs of approximately 100° as well as small size of $0.4 \times 0.4 \times 0.134 \, \lambda_0^3$ can be achieved simultaneously by the antenna element. In addition, high isolation of 33.6 dB can also be realized by introducing an air bridge. To further achieve high gain of approximately 11.22±0.66 dBi for both ports, an 1 × 4 antenna array is also designed. By adopting these measures, the proposed antenna is suitable for wide-coverage 5G microcell communications.

REFERENCES

[1] *Chinese Ministry of Industry and Information Technology Awarded 5G Licenses to Four Telecom Operators*. Accessed: Jun. 6, 2019. [Online]. Available: http://www.miit.gov.cn/n1146290/n1146402/n7039597/c7093441/content.html,

[2] W. An, Y. Li, H. Fu, J. Ma, W. Chen, and B. Feng, "Low-profile and wideband microstrip antenna with stable gain for 5G wireless applications," *IEEE Antennas Wireless Propag. Lett.*, vol. 17, no. 4, pp. 621–624, Apr. 2018.

[3] Y. Li, C.-Y.-D. Sim, Y. Luo, and G. Yang, "High-isolation 3.5 GHz eight-antenna MIMO array using balanced open-slot antenna element for 5G smartphones," *IEEE Trans. Antennas Propag.*, vol. 67, no. 6, pp. 3820–3830, Jun. 2019.

[4] J. Zhu, B. Peng, and S. Li, "Cavity-backed high-gain switch beam antenna array for 60-GHz applications," *IET Microw., Antennas Propag.*, vol. 11, no. 12, pp. 1776–1781, Sep. 2017.

[5] B. Feng, L. Li, J.-C. Cheng, and C.-Y.-D. Sim, "A dual-band dual-polarized stacked microstrip antenna with high-isolation and band-notch characteristics for 5G microcell communications," *IEEE Trans. Antennas Propag.*, vol. 67, no. 7, pp. 4506–4516, Jul. 2019.

[6] B. Feng, C. Zhu, J.-C. Cheng, C.-Y.-D. Sim, and X. Wen, "A dual-wideband dual-polarized magneto-electric dipole antenna with dual wide beamwidths for 5G MIMO microcell applications," *IEEE Access*, vol. 7, pp. 43346–43355, 2019.

[7] H. Wong, Q. W. Lin, H. W. Lai, and X. Y. Zhang, "Substrate integrated meandering probe-fed patch antennas for wideband wireless devices," *IEEE Trans. Compon., Packag., Manuf., Technol.*, vol. 5, no. 3, pp. 381–388, Mar. 2015.

[8] W. X. An, H. Wong, K. L. Lau, S. F. Li, and Q. Xue, "Design of broadband dual-band dipole for base station antenna," *IEEE Trans. Antennas Propag.*, vol. 60, no. 3, pp. 1592–1595, Mar. 2012.

[9] Y. Cui, X. Gao, H. Fu, Q.-X. Chu, and R. Li, "Broadband dual-polarized dual-dipole planar antennas: Analysis, design, and application for base stations," *IEEE Antennas Propag. Mag.*, vol. 59, no. 6, pp. 77–87, Dec. 2017.

[10] L. Ge and K. M. Luk, "Band-reconfigurable unidirectional antenna: A simple, efficient magneto-electric antenna for cognitive radio applications.," *IEEE Antennas Propag. Mag.*, vol. 58, no. 2, pp. 18–27, Apr. 2016.

[11] S.-W. Liao, Q. Xue, and J.-H. Xu, "A differentially fed magneto-electric dipole antenna with a simple structure," *IEEE Antennas Propag. Mag.*, vol. 55, no. 5, pp. 74–84, Oct. 2013.

[12] L. H. Ye, Y. F. Cao, X. Y. Zhang, Y. Gao, and Q. Xue, "Wideband dual-polarized omnidirectional antenna array for base-station applications," *IEEE Trans. Antennas Propag.*, vol. 67, no. 10, pp. 6419–6429, Oct. 2019.

[13] H. Zhang, S. Yang, Y. Chen, J. Guo, and Z. Nie, "Wideband dual-polarized linear array of tightly coupled elements," *IEEE Trans. Antennas Propag.*, vol. 66, no. 1, pp. 476–480, Jan. 2018.

[14] Y. Li and K.-M. Luk, "A linearly polarized magnetoelectric dipole with wide H-Plane beamwidth," *IEEE Trans. Antennas Propag.*, vol. 62, no. 4, pp. 1830–1836, Apr. 2014.

[15] G. Yang, J. Li, J. Yang, and S.-G. Zhou, "A wide beamwidth and wideband magnetoelectric dipole antenna," *IEEE Trans. Antennas Propag.*, vol. 66, no. 12, pp. 6724–6733, Dec. 2018.

[16] B. Feng, X. He, J.-C. Cheng, Q. Zeng, and C.-Y.-D. Sim, "A low-profile differentially fed dual-polarized antenna with high gain and isolation for 5G microcell communications," *IEEE Trans. Antennas Propag.*, vol. 68, no. 1, pp. 90–99, Jan. 2020.

[17] J. Zhu, S. Li, S. Liao, and Q. Xue, "Wideband low-profile highly isolated MIMO antenna with artificial magnetic conductor," *IEEE Antennas Wireless Propag. Lett.*, vol. 17, no. 3, pp. 458–462, Mar. 2018.

[18] X. Ren, S. Liao, and Q. Xue, "A differentially fed dual-polarized magnetic dipole antenna for spaceborne applications," *IEEE Trans. Antennas Propag.*, vol. 67, no. 2, pp. 861–871, Feb. 2019.

[19] J. Lai, B. Feng, and Q. Zeng, "A dual-polarized wide-beamwidth magneto-electric dipole antenna for the fifth generation mobile communications," in *Proc. IEEE 6th Int. Symp. Electromagn. Compat. (ISEMC)*, Nov. 2019, pp. 1–3.

[20] *HFSS: High Frequency Structure Simulator Based on the Finite Element Method*. Accessed: Jun. 6, 2019. [Online]. Available: https://www.ansys.com

[21] C. A. Balanis, *Antenna Theory: Analysis and Design*. Hoboken, NJ, USA: Wiley, 2016.

[22] H. Wong, K.-M. Mak, and K.-M. Luk, "Wideband shorted bowtie patch antenna with electric dipole," *IEEE Trans. Antennas Propag.*, vol. 56, no. 7, pp. 2098–2101, Jul. 2008.

BOTAO FENG (Senior Member, IEEE) was born in Guangdong, China, in 1980. He received the B.S. and M.S. degrees in communication engineering from the Chongqing University of Posts and Telecommunications (CQUPT), Chongqing, China, in 2004 and 2009, respectively, and the Ph.D. degree in communication and information system from the Beijing University of Posts and Telecommunications (BUPT), Beijing, China, in 2015.

Since February 2020, he has been an Adjunct Senior Research Fellow with the Energy Materials Telecommunications (EMT) Research Centre, Institut National de la Recherche Scientifique (INRS), Canada. He is currently the Head of the Laboratory of Wireless Communication, Antennas and Propagation and the Deputy Director of the Department of Electronic Science and Technology, Shenzhen University, and the President of Shenzhen Taobida Technology Company Ltd. He and his research team members are currently conducting over ten projects on antenna development and design for 5G/THz and future communications, which are supported by natural science research funds and industrial cooperation research and development funds. His several antenna designs for 5G applications have been widely used by Chinese communication operators. It is estimated that the related total production value is approximately 200 million Ren Min Bi (RMB). He has authored or coauthored more than 60 Science Citation Index (SCI) and Engineering Index (EI) articles. He holds over 20 invention patents. His research interests include antennas and mobile communications.

Dr. Feng serves as a Regular Peer Reviewer, a Technical Committee Member, the General Chair, and a Guest Editor for IEEE/IET, Elsevier, Wiley, and Springer journals and conferences on microwave technique and antenna development. He also serves concurrently as a Senior Evaluation Expert of Degree and Graduate Education Center of the Chinese Ministry of Education, the Natural Science Foundation Committee of Guangdong Province, the Information and Communication Technologies Senior Title Evaluation Committee of Guangdong Province, the Science and Technology Innovation Committee of Shenzhen City, and so on. He received the award of the Outstanding Instructor of the First Prize in National Graduate Electronic Contest, the Tencent Outstanding Teacher Award, and so on.

JIEXIN LAI was born in Zhanjiang, Guangdong, China, in 1993. He received the B.S. and M.S. degrees from Shenzhen University, in 2016 and 2020, respectively. His research interests include base-station antenna and indoor antenna.

CHOW-YEN-DESMOND SIM (Senior Member, IEEE) was born in Singapore, in 1971. He received the B.Sc. degree from the Engineering Department, University of Leicester, U.K., in 1998, and the Ph.D. degree from the Radio System Group, Engineering Department, University of Leicester, in 2003.

From 2003 to 2007, he was an Assistant Professor with the Department of Computer and Communication Engineering, Chienkuo Technology University, Changhua, Taiwan. In 2007, he joined the Department of Electrical Engineering, Feng Chia University (FCU), Taichung, Taiwan, as an Associate Professor, where he became a Full Professor in 2012 and a Distinguish Professor in 2017. He has served as the Executive Officer of Master's Program with the College of Information and Electrical Engineering (Industrial Research and Development) and the Director of the Intelligent IoT Industrial Ph.D. Program from August 2015 to July 2018. He is currently serving as the Head of the Department of Electrical Engineering and the Director of the Antennas and Microwave Circuits Innovation Research Center, Feng Chia University. He has authored or coauthored over 130 SCI articles. His current research interests include antenna design, VHF/UHF tropospheric propagation, and RFID applications.

Dr. Sim He is a Fellow of the Institute of Engineering and Technology (FIET), a Senior Member of the IEEE Antennas and Propagation Society, and a Life Member of the IAET. He served as the TPC Member for the APMC 2012, the APCAP 2015, IMWS-Bio 2015, CSQRWC 2016, ICCEM 2017, APCAP 2018, CIAP 2018, and APMC 2019. He was a recipient of the IEEE Antennas and Propagation Society Outstanding Reviewer Award (IEEE Transactions on Antennas and Propagation) for six consecutive years 2014–2019. He received the Outstanding Associate Editor Award from the IEEE Antennas Wireless and Propagation Letters, in July 2018. He has also served as the TPC Sub-Committee Chair (Antenna) for the ISAP 2014, PIERS 2017, and PIERS 2019. He was invited as the Workshop/Tutorial Speaker at APEMC 2015, iAIM 2017, and InCAP 2018 and an Invited Speaker of TDAT 2015, iWAT 2018, APCAP 2018, and ISAP 2019. He was the Keynote Speaker of SOLI 2018. He has served on the Advisory Committee of InCAP 2018/2019. He has served as the TPC Chair for APCAP 2016 and iWEM 2019. He has also served as the Chapter Chair of the IEEE AP Society, Taipei Chapter, from January 2016 to December 2017. He has been the Founding Chapter Chair of the IEEE Council of RFID, Taipei Chapter, since October 2017. He is also serving as the Associate Editor for the IEEE AWPL, IEEE Access, the IEEE Journal of Radio Frequency Identification, and the *International Journal of RF and Microwave Computer-Aided Engineering* (Wiley). Since October 2016, he has been serving as the Technical Consultant for the Securitag Assembly Group (SAG), which is one of the largest RFID tag manufacturers in Taiwan.

• • •